International Communications in Heat and Mass Transfer 165 (2025) 109079

Contents lists available at ScienceDirect

International Communications in Heat and Mass Transfer

journal homepage: www.elsevier.com/locate/ichmt

Evaporation in electrohydrodynamic atomisation: A numerical and experimental investigation

Ngoc Luan Mai [a,*], Trung Hieu Vu [a], Hoai-Duc Vu [a], Canh Doan [a], Yuen Yong [b,*], Thien Xuan Dinh [c], Dzung Viet Dao [a], Van Thanh Dau [a,*]

[a] School of Engineering and Built Environment, Griffith University, Queensland, Australia
[b] School of Engineering, The University of Newcastle, NSW, Australia
[c] The Commonwealth Scientific and Industrial Research Organisation, Australia

ARTICLE INFO

Keywords:
Numerical methods
Evaporation
Electrospray
Electrohydrodynamic atomization
Experiments
Particle morphology

ABSTRACT

In this paper, the influence of evaporation in electrohydrodynamic atomization (electrospray) is numerically and experimentally investigated. The simulation was performed utilizing the Taylor-Melcher's leaky-dielectric model and the d^2 Law to simulate thermophysical processes in electrospray. Experiments were conducted to validate the numerical approach and to investigate the influence of evaporation on particle morphology. Results by simulations are consistent with experiments, showing agreement in both Taylor-cone captured by high-speed camera and vapour field visualized by Schlieren imaging. Experiments on different solvents suggest major impacts of interelectrode distance on the residual solvent on the collected particles. However, these impacts were less significant on particle size and morphology particularly when using solvents with medium to low volatility. Particle size is found to increase with temperature and solvent volatility, confirming the correlation reported in literature. Moreover, evaporation was determined to have limited effect on the overall shape of the Taylor-cone and spray jet, due to inherently high vapour concentration around the nozzle vicinity. These contributions will improve the understanding of evaporation process in electrospray and offer useful guidelines for optimizing the technique, particularly in situations where evaporation is a key factor controlling particle size and minimizing harmful residue.

1. Introduction

Electrohydrodynamic atomization (EHDA), or electrospray, is a technique that produces charged droplets from a liquid solution by applying high voltage onto a nozzle's tip, creating an intense electric field that can break the liquid into micro and sub-microscale droplets. Electrospray has found applications in various fields, including food processing [1,2], fuel spray and combustion [3,4], electric propulsion [5,6], cooling [7,8] and pharmaceutics [9–11]. A closely related technology, electrospinning, where the liquid involved often possess high viscosity and viscoelasticity so that the jet can be kept in continuous form to produce fibres instead of droplets [12]. Electrospun fibres has been proven useful in a wide range of applications, such as tissue engineering [13], filtration [14], biosensors and affinity membrane [15], protective clothing [16], smart textile and garment [17,18], energy storage and conversion [19,20], and jet printing [21] due to its controllability in size, morphology, structure, and shapes.

The single cone-jet mode is the most used working regime in electrospray or electrospinning for its stability, controllability, and high yield rate. In the cone-jet mode, the liquid forms a conical shape, known as Taylor-cone, from which a jet is emitted and then broken into small droplets. Due to the residual charge concentration in the droplets and the continuous effect of electric field, these small droplets are broken into smaller droplets in a process named Coulomb fission. Fig. 1 illustrates the working principles of EHDA showing the Taylor-cone, jet, Coulomb fission and evaporation region accompanied by different applications of electrospray/electrospinning.

Evaporation of solvents is a crucial factor in Coulomb fission where it dictates division of the electrosprayed droplets [22] or the quality and the toxicity of electrospun fibres [12]. Despite being an important element, evaporation is insufficiently investigated. Smith et al. [23] presented an experimental technique to measure the size and charge of individual droplets using phase Doppler interferometry. The authors were able to monitor the temporal evolution of the droplet size which is dominated by evaporation. Wilhelm et al. [24] proposed a theoretical

* Corresponding authors.
E-mail addresses: luan.mai@griffithuni.edu.au (N.L. Mai), yuenkuan.yong@newcastle.edu.au (Y. Yong), v.dau@griffith.edu.au (V.T. Dau).

https://doi.org/10.1016/j.icheatmasstransfer.2025.109079

Available online 20 May 2025

Nomenclature

Regular letters:

d_j	jet diameter, μm
l_c	cone length, mm
$\boldsymbol{E}$	electric field, $-\nabla\phi$
$\boldsymbol{f}_e$	electrostatic force, N/m^3
$\boldsymbol{f}_\sigma$	surface tension force, N/m^3
$\boldsymbol{g}$	gravitational acceleration, m/s^2
$i.d$	inner diameter, mm
$o.d$	outer diameter, mm
$\boldsymbol{J}$	current density, A/m^2
p	pressure, Pa
Q	liquid low rate, ml/h
r_E	interelectrode distance, mm
t	time, s
$\boldsymbol{u}$	fluid velocity, m/s
$\boldsymbol{u}_r$	artificial compression term
c_p	specific heat capacity, J/kgK
T	temperature, K
$\boldsymbol{S}$	source term
$\widehat{m_i}$	mass transferred from liquid to vapour, kg/sm^2
C	model coefficient
$D_{v,i}$	diffusion coefficient
Y	mass fraction
Le	Lewis number
M	molar masses
p_{sat}	saturation pressure, bar or Pa
A, B, C	Antoine coefficients
ΔH_{vap}	latent heat of vaporisation, kJ/kg
Q	flow rate

Greek letters:

γ_{liq}	phase fraction of liquid
ε	permittivity, F/m
ε_0	permittivity of free space
ε_r	dielectric constant
μ	fluid viscosity, Pa.s
φ_c	cone angle, $^\circ$
κ	mean curvature of the free surface, m^{-1}
κ_e	electrical conductivity of the fluid, S/m
μ_e	mobility of charge of the gas
ρ,	fluid density, kg/m^3
ρ_g	gas density, kg/m^3
ρ_e	volumetric charge density, C/m^3
σ	surface tension, N/m
ϕ	electric potential, V
φ_c	cone angle
λ	thermal conductivity, W/mK

Abbreviations:

EHDA	electrohydrodynamic atomization
VOF	volume of fluid
CSF	continuum surface force
DMF	dimethylformamide
PVDF	polyvinylidene fluoride
SEM	scanning electron microscope

Subscripts:

v	vapour
g	gas

model to investigate the transport, evaporation and deposition of electrosprayed droplets on a heated substrate to predict the production of electrolyte films for solid oxide fuel cells. The results suggest that evaporation does not significantly affect droplet transport, but it increases the salt concentration due to reduced droplet size, which causes damage to the film quality. The influence of evaporation on the morphology and solidification of electrospun poly(ethylene oxide) aqueous solution was investigated by Tripatanasuwan et al. [25]. They

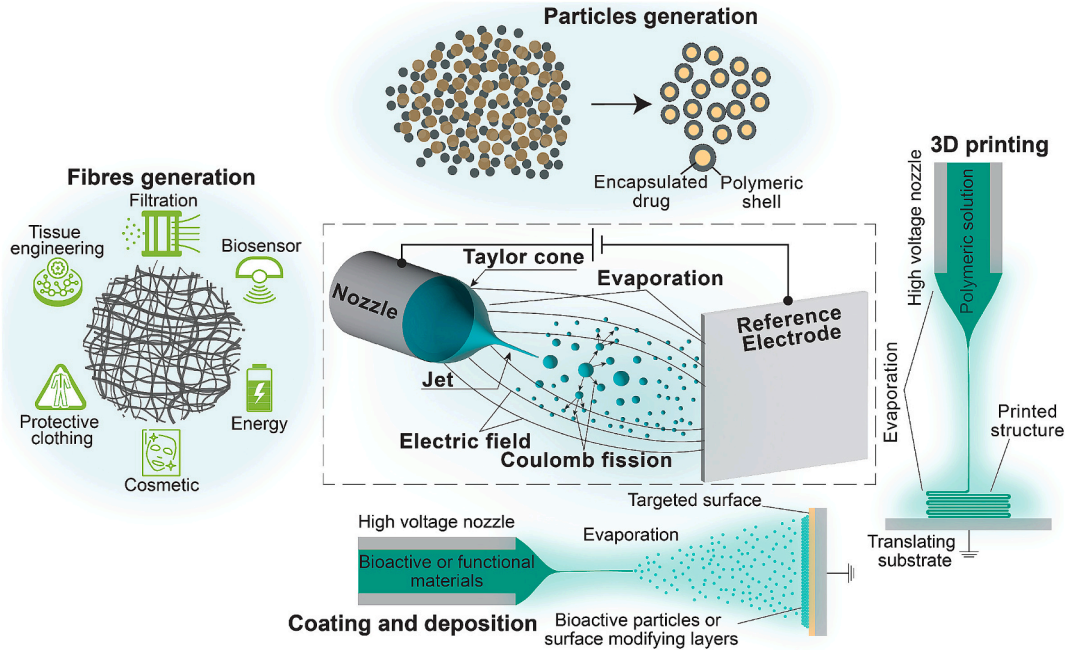

Fig. 1. Illustration of EHDA working principles and its various prominent applications.

concluded that thinner fibres can be created by reducing evaporation rate through controlling relative humidity. The correlation between fibre diameter and evaporation rate was later reaffirmed by Cai and Gevelber [26] and Golecki [27]. Meng et al. [28] introduced a modified electrospray process for the preparation of poly lactic-*co*-glycolicacid microparticles. This work concluded that rapid evaporation of solvent restrains the droplet fission, while the increase of solvent vapour pressure was found to prolong jet thinning and reduce collected particles' size [28]. A similar correlation between particles' size and solvent evaporation was reported by Jafari-Nodoushan et al. [29]. The authors further found out that cup-like and more porous microparticles can be produced with more volatile solvents [29]. Vu et al. [30] utilised a chamfered nozzle to create a nonuniform evaporation rate at the nozzle's outlet, preventing clogging and improving the uniformity of particles and fibres. Molecular dynamics simulations were recently employed to investigate the effects of evaporation in electrospray by Li et al. [31] showing temperature rise can weaken the bonds between molecules and yield a larger number of broken droplets. This work [31], however, did not study the influences of evaporation on the morphology of the sprayed particles.

This paper presents a comprehensive numerical and experimental analysis on evaporation in electrohydrodynamic atomization, focusing on the behaviors of electrospray process and generated particles. The study provides an in-depth understanding of the evaporation dynamics in electrohydrodynamic atomization and guidelines for optimizing the process. This is beneficial to electrospray applications such as pulmonary drug delivery where controlling the morphology of the particle is important for optimal drug efficacy.

The numerical model presented in this work is developed in OpenFOAM. It is constructed based on the Taylor-Melcher's leaky-dielectric model and the d^2 Law to simulate the electrohydrodynamic and mass transfer processes. Electrospray experiments were carried out to validate simulation results and to investigate the influence of evaporation on the morphology of polymeric particles. Simulation results showed reasonable agreement with experiments in terms of Taylor-cone's geometric characteristics captured by high-speed camera and vapour field visualisation technique using Schlieren imaging method. Particle morphology analyses suggest that the interelectrode distance has negligible impact on the particle size and morphology, yet the interelectrode distance influences the amount of residual solvents in the collected particles in certain cases. The analyses also show that the size of particles increases with evaporation rate but independent to temperature changes. Both simulations and experiments show that Taylor-cone and jet's shape is independent with temperature, implying that evaporation is solely influential in the Coulomb fission region.

2. Experiment apparatus

2.1. Electrospray

Two set of electrospray experiments, namely the pure-solvent electrospray and polymeric solutions electrospray, were conducted to validate the reliability of the numerical solver and investigate the morphology of polymeric particles with different evaporation rates. In the pure-solvent cases, the point-to-plane configuration was employed, whilst the point-to-drum configuration was used for the polymeric solutions. Fig. 2 shows the illustration of the experimental setup of both cases.

For the electrospray of pure solvents, we used Acetone (Sigma Aldrich, ≥99.5 %), Ethanol (Sigma Aldrich, ≥99.5 %) and Dimethylformamide (DMF - Sigma Aldrich, ≥99 %) as spraying liquids. The liquids were delivered by a syringe pump (New Era) at flow rate $Q = 1.5$ mL/h to the tip of a stainless-steel nozzle (Gauge 30 - Musashi Engineering, Inc., Japan, i.d. = 0.159 mm, o.d. = 0.312 mm). The nozzle is connected to a high-voltage DC power supply (Gamma High Voltage Research). The distance between the nozzle and the grounded plane

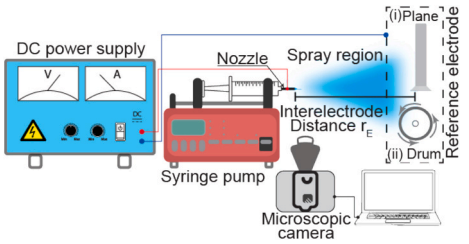

Fig. 2. Schema of electrospray experimental setup. The nozzle (gauge 30 or 22) is connected to positive high voltage. The grounded plane electrode or rotational drum electrode is used as reference electrodes to conduct pure-solvent electrospray and polymeric solutions electrospray, respectively. The interelectrode distance r_E is measured from the top of the nozzle to the surface of the plane electrode or the rotational center of the drum.

electrode was fixed at $r_E = 5$ mm for all cases. To capture the shape of the Taylor-cone, a high-speed camera with microscopic view (HHC X9 Pro, Mega Speed, USA) was used.

For the electrospray of polymeric solutions, 3 % *w*/w (weight/weight) of polyvinylidene fluoride (PVDF – Sigma Aldrich, average $M_w \sim 534{,}000$) was dissolved into pure Acetone, DMF and a mixture of Acetone and DMF (*w*/w of 1:1) to form three different solutions with different vapour pressures. The solution was sprayed with gauge 22 nozzle (i.d. = 0.413 mm, o.d. = 0.718 mm) in 20 min while the drum electrode, covered with NiCu tape, rotated at 1300 rpm approximately. Three separated samples of electrosprayed particles were then extracted at different locations on the collector and analysed by a scanning electron microscope (SEM – Thermo Fisher Scientific) and the ImageJ image processing program. In additional, the impact of temperature on the morphology of particles was investigated using point-to-drum electrospray with PVDF 3 % in Acetone 1:1 DMF solution. The interelectrode distance was set at $r_E = 8$ cm, and the temperatures were regulated at $T = 35$ °C and 45 °C using a syringe heater.

2.2. Schlieren imaging

Schlieren imaging is used to visualise optical inhomogeneities that are transparent to the human's eyes [32]. The applications for this technique include shock imaging, supersonic jets visualisation, ball lightning and explosion imaging [33]. Recently, there have been reports of this technique in visualising the vapour field from the plume of electrosprayed droplets [34,35]. Since the evaporated vapour field is a crucial part of solvent evaporation process in electrospray, we utilised the Schlieren technique in this study to examine the behaviour of the vapour field of different liquids and to validate the simulation results as shown in Fig. 3. A concave mirror (diameter 50 mm, focal length 200 mm), a light source and a razor blade were added to the point-to-plane electrospray configuration. The light was directed through the spray region which included the Taylor-cone, jet and the sprayed plume. Due

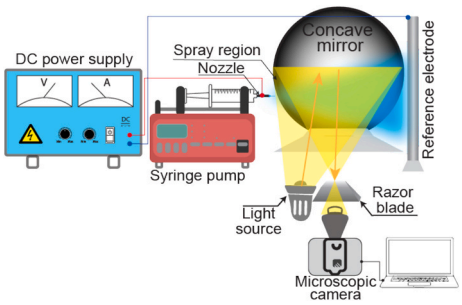

Fig. 3. Schema of Schlieren experiment installation. The point-to-plane configuration with the addition of a light source, a razor blade and a concave mirror.

to the difference in refractive index of the liquid and vapour field, the light bends differently as it passes through these liquid and vapour. The spherical mirror functions to reflect and focus light from a point source, subsequently forming an image on the high-speed camera sensor (HHC X9 Pro, Mega Speed, USA). The razor blade, placed at the mirror focal point, selectively blocked the stray light, preventing them from reaching the camera sensor and simultaneously increase the image contrast. Thus, the vapour field would appear to be darker than the air in the resulted images. This experiment was conducted on Acetone, Ethanol and DMF (see Table. 1 for relevant properties) to contrast their vapour plume. To obtain the best vapour field visualisation, a high flow rate of $Q = 4$ mL/h and the Gauge 17 nozzle (i.d. = 1.067 mm, o.d. = 1.473 mm) with an interelectrode distance of $r_E = 5$ cm were used.

3. Simulation model

3.1. Governing equations

The Taylor-Melcher's leaky-dielectric model [36,37] was implemented to simulate the fluid dynamics and electrostatic regimes in electrospray. To consider the thermophysical behaviour and mass transfer of liquid evaporation, the energy equation was solved accompanied by a diffusion evaporation model based on the d^2 Law [38] which is provided by the OpenFOAM package.

3.1.1. Fluidic field

For the fluidic field, the continuity and momentum equations are considered,

$$\frac{\partial \rho}{\partial t} + \nabla\cdot(\rho \boldsymbol{u}) = 0, \tag{1}$$

$$\rho\left[\frac{\partial \boldsymbol{u}}{\partial t} + (\boldsymbol{u}\cdot\nabla)\boldsymbol{u}\right] = -\nabla p + \eta\nabla^2\boldsymbol{u} + \boldsymbol{f}_\sigma + \boldsymbol{f}_e + \rho\boldsymbol{g}, \tag{2}$$

where ρ represents fluid density, t denotes time, $\boldsymbol{u}$ is the fluid velocity, p stands for the pressure, η is the fluid viscosity, and $\boldsymbol{g}$ corresponds to the gravitational acceleration. The two force terms $\boldsymbol{f}_\sigma$ and $\boldsymbol{f}_e$ indicate the surface tension force and electrostatic force, respectively. In OpenFOAM, the surface tension force is calculated per unit volume by the continuum surface force (CSF) model [39],

$$\boldsymbol{f}_\sigma = \sigma\kappa\nabla\gamma_{liq} = -\sigma\nabla\cdot\left(\frac{\nabla\gamma_{liq}}{|\nabla\gamma_{liq}|}\right)\nabla\gamma_{liq}, \tag{3}$$

where σ is the surface tension, κ represents the mean curvature of the free surface, the phase fraction of liquid γ_{liq} is determined using the VOF method to capture the interface in the inhomogeneous fluid field [40]. This approach is combined with a secondary convection term to enhance the resolution of the interface,

$$\frac{\partial \gamma_{liq}}{\partial t} + \nabla\cdot\left(\gamma_{liq}\boldsymbol{u}\right) + \nabla\cdot\left(\gamma_{liq}\left(1-\gamma_{liq}\right)\boldsymbol{u_r}\right) = 0, \tag{4}$$

where $\boldsymbol{u_r}$ is an artificial compression term applied to achieve higher interface resolution [41]. Fluid density and viscosity are determined through arithmetic averaging based on the phase fraction,

$$\begin{aligned}\rho &= \rho_1\gamma_{liq} + \rho_2\left(1-\gamma_{liq}\right),\\ \mu &= \mu_1\gamma_{liq} + \mu_2\left(1-\gamma_{liq}\right).\end{aligned} \tag{5}$$

3.1.2. Electrostatic field

In the electrostatic regime, the governing equations are solved iteratively to calculate the electrostatic force $\boldsymbol{f}_e$. The magnetic induction is neglected in the equations. The process begins with the solution of Gauss's law,

$$\nabla\cdot(\varepsilon\boldsymbol{E}) = \rho_e. \tag{6}$$

By integrating Eq. 6 with the expression $\boldsymbol{E} = -\nabla\phi$, the Poisson's equation for electrostatics is formulated,

$$\nabla^2(\phi) = \frac{-\rho_e}{\varepsilon}, \tag{7}$$

where ε represents the permittivity of the fluids, ϕ is the electric potential, and ρ_e is the volumetric charge density. This is followed by the conservation of charge,

$$\frac{\partial \rho_e}{\partial t} + \nabla\cdot\boldsymbol{J} = 0, \tag{8}$$

where $\boldsymbol{J}$ denotes the current density and is expressed as the combination of ohmic charge conduction and charge convection within the fluid flow, hence Eq. 8 can be rewritten as,

$$\frac{\partial \rho_e}{\partial t} + \nabla\cdot(\rho_e\boldsymbol{u}) + \nabla\cdot(\kappa_e\boldsymbol{E}) = 0, \tag{9}$$

where κ_e represents the electrical conductivity of the fluid. Both electrical conductivity and permittivity are defined using harmonic averages across the computational domain, a method that has proven to be more reliable in electrohydrodynamic simulations compared to arithmetic averaging [42],

$$\begin{aligned}\frac{1}{\varepsilon} &= \frac{\gamma_{liq}}{\varepsilon_1} + \frac{1-\gamma_{liq}}{\varepsilon_2},\\ \frac{1}{\kappa_e} &= \frac{\gamma_{liq}}{\kappa_{e1}} + \frac{1-\gamma_{liq}}{\kappa_{e2}}.\end{aligned} \tag{10}$$

For incompressible fluids, the electrostatic force is the combined effect of the Coulombic force and the polarization force, which arise from the presence of interfacial charges and the inhomogeneity of the fluid field [43],

$$\boldsymbol{f}_e = \rho_e\boldsymbol{E} - \frac{1}{2}|\boldsymbol{E}|^2\nabla\varepsilon. \tag{11}$$

3.1.3. Thermophysical and evaporation mass transfer model

Firstly, the incompressible energy equation is solved to obtain the temperature field,

$$\frac{\partial}{\partial t}\left(\rho c_p T\right) + \nabla\bullet\left(\rho c_p \boldsymbol{u} T\right) = \nabla\bullet\left(\lambda\nabla T\right) + \boldsymbol{S}, \tag{12}$$

where the left-hand-side includes the temporal derivative and the convective transport of internal energy $e = c_p T$, and the right-hand-side

Table 1
Physical properties of air, Acetone, Ethanol and DMF.

Fluid	Air	Acetone	Ethanol	DMF
Density ρ (kg/m^3)	1.225	784	800	944
Dynamic Viscosity μ (Pa.s)	1.8×10^{-5}	3.06×10^{-4}	1.1×10^{-3}	0.796×10^{-3}
Surface tension σ (N/m)	NaN	0.0245	0.022	0.037
Dielectric constant ε_r	1	20.7	23	36.7
Electric conductivity κ_e (mS/m)	1×10^{-9}	2×10^{-5}	5.1×10^{-6}	1.6×10^{-4}
Specific heat capacity c_p (J/kgK)	900	2140	2570	2060
Latent heat of vaporisation ΔH_{vap} (kJ/kg)	NaN	534	846	639
Antoine coefficients (A, B, C)	NaN	4.42448 1312.253 −32.445	5.24677 1598.67 −46.424	3.93068 1337.716 −82.648
Saturation pressure p_{sat} at 25°C (bar)	NaN	0.3	0.08	0.005
Thermal conductivity λ (W/mK)	0.02624	0.18	0.151	0.19

shows the conductive transport and source term $\boldsymbol{S}$.

The d^2 Law gives the following mass transfer formulation,

$$\widehat{m_i} = -C\rho_g D_{v,i} \frac{\frac{dY_{v,i}}{dn}}{1 - \sum_1^{N_v} Y_{g,j}}, \tag{13}$$

in which $\widehat{m_i}$ is the mass transferred from liquid to vapour, $C = 1$ is the model coefficient by default, ρ_g represents gas phase density, $\frac{dY_{v,i}}{dn}$ is the normal derivative of evaporated component. The diffusion coefficient $D_{v,i}$ is calculated by,

$$D_{v,i} = \frac{\lambda}{Le\rho c_p}, \tag{14}$$

where Le is the Lewis number, equals to unity. The saturated vapour mass fraction $Y_{g,j}$ is determined from,

$$Y_{g,j} = \frac{1}{1 + \left(\frac{p}{p_{sat}} - 1\right)\frac{M_g}{M_v}}. \tag{15}$$

Here, p_{sat} is the saturation pressure of liquid, M_g and M_v are respectively the molar masses of the ambient air and vapour phases. Saturation pressure p_{sat} is calculated using the Antoine equation,

$$\log_{10}(p_{sat}) = A - \frac{B}{C + T}, \tag{16}$$

where A, B and C are Antoine coefficients which are liquid property, and T is temperature which can be determined from solving Eq. 12.

3.2. Schema, mesh and boundary conditions

The electrostatic and fluid-dynamics solver are solved consecutively with the evaporation phase change calculations each timestep. A detailed description of the solving procedure is presented in Fig. 4(a). Simulations in this study employ the computational domain built in accordance with the pure-solvent experimental setups described in Section 2.1. Fig. 4(b) shows the computational mesh and the relevant dimensional annotations. The nozzle boundary is applied with constant voltage $\phi = \phi_0$, while the reference plane electrode is set with $\phi = 0$ V. The atmospheric boundaries enclose the domain and assigned with far-field conditions. We used the axisymmetric 2-D model to simplify the solution and reduce the computational costs, with a 5° wedge condition for the front and back patches. Additional information on simulation model is provided in Supplementary Material S1. Moreover, the relevant physical and thermophysical properties of air and the liquids used in this study are shown in Table 1.

4. Results and discussion

4.1. Evaporation model validation

Experiment and simulation on the natural evaporation of an Acetone droplet at room conditions were conducted to verify the evaporation model. Acetone is a highly volatile liquid, evaporating quickly when placed in normal atmospheric conditions. The simulation of the evaporation of a similar droplet was carried out using the presented models and properties listed in Table. 1.

Fig. 5(a) graphs the volume of the Acetone droplet in simulation and experiment at different timesteps with inset illustrating the experimental setup. Solidworks (Dassault Systèmes) was used to reconstruct and measure the volume of the 3-dimensional Acetone droplet from the captured droplet's profiles. The acquired results show good correlation between experiment and simulation, with an average error of roughly 18 % for the whole period. It is worth noting that the experimental droplet evaporation rate in both cases reduced at the droplet shrunk, indicated by the steepness of the plot lines. This trend can be explained by the decrease in surface area of the droplet which is a key factor affecting the evaporation rate of liquid droplets [44]. However, the evaporation rate of experimental droplet was higher in the first half period ($t < 35$ s), and lower in the second half period ($t > 35$ s). These differences caused the peak in error at $t = 30$s and yielded excellent agreements at the last few timesteps ($t = 60, 65, 70$s). Possible factors accounting for these differences are the inaccuracy in experimental angle setup and image processing. Moreover, the current numerical model does not consider relative humidity which is generally known to be inversely proportional with evaporation rate of liquids [45,46]. Nevertheless, the numerical model provides a good agreement with experimental data and will be used to simulate the evaporation process of electrospray.

4.2. Validation of evaporation in electrospray simulation model

Acetone, Ethanol and DMF with high, medium and low volatility respectively and distinct evaporation rates (see saturation pressure in Table 1) were electrosprayed experimentally. The evaporated vapour field in the vicinity of the Taylor-cone and jet region was visualized using the Schlieren imaging method described in Section 2.

Fig. 6 shows results acquired from the electrospray experiment and simulation of Acetone, Ethanol and DMF, respectively. Experimental results in Figs. 6(i, a-c) indicate that the liquids require different voltage conditions ($\phi_{Acetone} = 2300$ V; $\phi_{Ethanol} = 2100$ V; $\phi_{DMF} = 3000$ V) to establish a stable cone-jet mode due to the difference in surface tension (Table 1). As the cone-jet mode is maintained by an equilibrium between electrostatic force and the surface tension force [47], higher surface tension requires stronger electric field. This behaviour is supported by

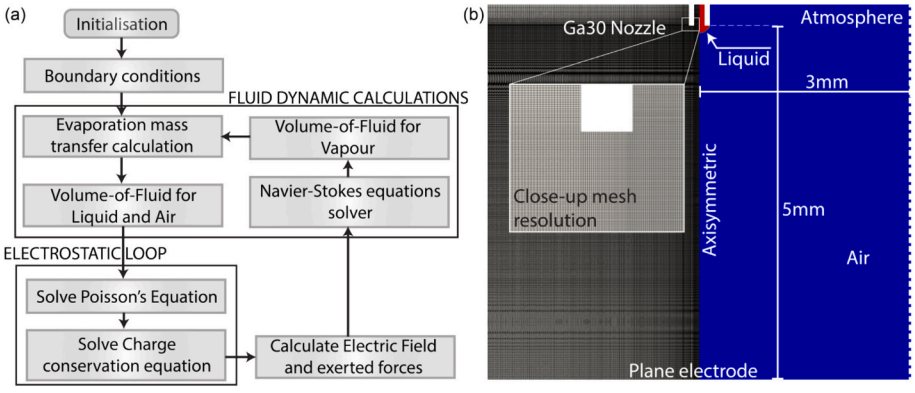

Fig. 4. (a) Flowchart of the numerical solver for electrospray with evaporation model; (b) The axisymmetric mesh model with dimensional and boundary annotations. Inset figure shows close-up view of the mesh resolution nearby the nozzle.

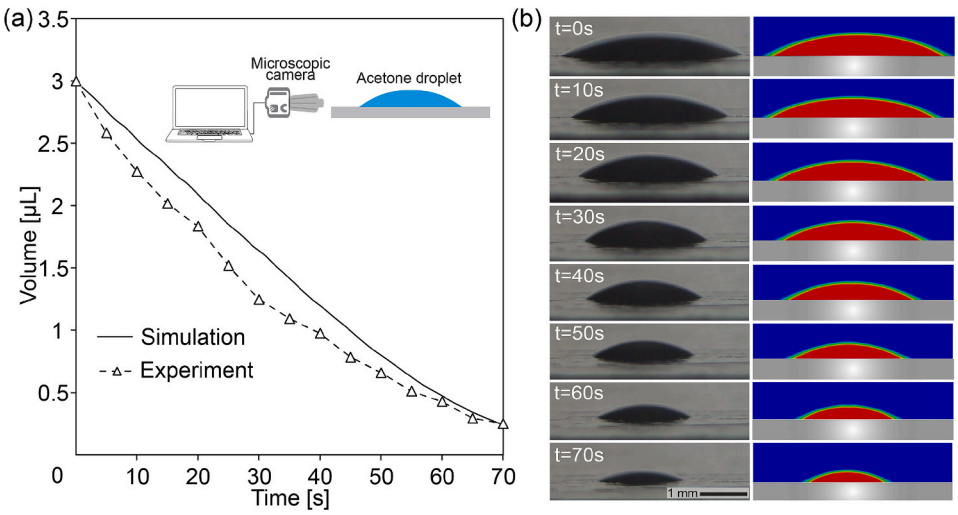

Fig. 5. (a) The correlation between simulation and experiment results of the acetone droplet evaporation, a droplet of Acetone (~3 μL) was dropped onto a Teflon surface and captured the volumetric reduction of the droplet over 70 s by a microscopic (Hayear Electronics) camera; (b)Time-interval images of acetone droplet in experiment and simulation, scale bar is valid for all time steps.

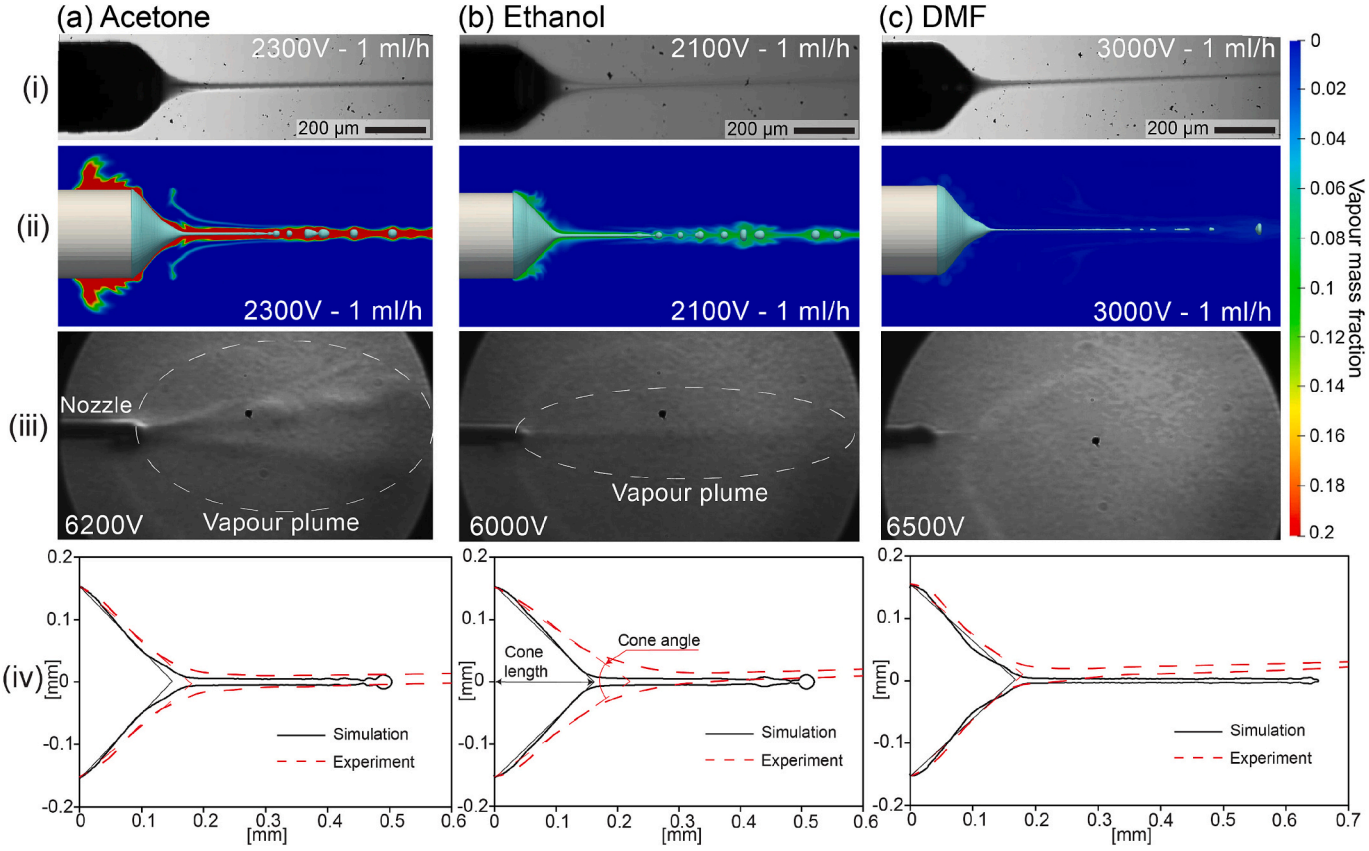

Fig. 6. Simulation and experiment results of Taylor-cone in electrospray of different liquids: (a) Acetone; (b) Ethanol; and (c) DMF. Results include: (i) Taylor-cone and jet shape; (ii) Simulated Taylor-cone and jet shape with evaporated vapour contour; (iii) Evaporated vapour visualized by the Schlieren method, with the dark areas in the plume indicating the presence of the vapour field; and (iv) Comparison of Taylor-cone shape and jet region between simulation and experiment.

the simulated result Fig. 6(ii, a-c) which yield stable cone-jet mode at the same voltage conditions with experiments. Furthermore, the vapour field contour from simulations also demonstrates a reasonable agreement with Schlieren visualisations (Fig. 6(iii)) which display very distinguishable vapour plumes for the three liquids. For Acetone, simulation yields dense vapour field adjacent to the cone and jet region (Fig. 6(a-ii)), whilst Schlieren visualisation shows a wide and thick vapour plume emitted from the nozzle (Fig. 6(a-iii)). With lower vapour pressure, Ethanol has significantly less vapour field concentration in simulation and narrower vapour plume in Schlieren visualisation (Figs. 6(b-ii&iii)). Finally, the vapour field can hardly be seen in both experiment and simulation for DMF (Fig. 6(c-ii) and Fig. 6(c-iii)). However, due to the limitations in sensitivity of the Schlieren method, the vapour field of the DMF case may be underestimated and appears

invisible in Fig. 6(c-iii). Future upgrades and calibrations to the experimental apparatus can be implemented to enhance the resolution of the visualisations [48]. Videos of Schlieren visualisation are provided in the Supplementary Materials Videos.

The Taylor-cone's length l_c and angle φ_c obtained from the simulation and experiment results in Figs. 6(iv) are compared in Table 2. In generally, the empirical cone's length is larger than that of the numerical but the empirical cone's angles are smaller compared to simulations in all three cases. For Acetone, the measured cone length and angle have a deviation of 17.33 % and 15 %, respectively, while for Ethanol, these deviations are higher, which are 27 % and 24 % for length and angle respectively. Finally, the DMF case yields the highest agreement, marking a roughly 7 % and 5 % for length and angle differences, respectively. Similarly to the validation in Fig. 5, the deviations between simulation and experiment could be attributed to the lack of humidity consideration in the evaporation model. Furthermore, the employed axisymmetric 2-D mesh model with simplified boundary conditions and incompatible charge interpolation scheme. Future improvements such as the implementation of relative humidity in the d^2 Law [49], 3D simulations and other charge interpolation schemes [41] can be carried out to enhance the accuracy of the numerical method. Nevertheless, the proposed numerical model has achieved acceptable agreement with experiments in both qualitative and quantitative analyses for all three liquids, further consolidating the potential of simulations for evaporation in electrospray.

4.3. Morphology of polymeric particles electrosprayed with different conditions

In this section, we analyse the morphology of the PVDF particles electrosprayed at room temperature (25 °C) with three different interelectrode distance r_E (8 cm, 12 cm and 16 cm) to investigate the effects of evaporation in electrospray. The particle size distribution for PVDF 3 % in Acetone, PVDF 3 % in Acetone 1:1 DMF solution and PVDF 3 % in DMF solution are plotted in Fig. 7.

Results of PVDF 3 % in Acetone are shown in Fig. 7(a-c). Particle sizes are relatively similar across the three cases of r_E (8 cm, 12 cm and 16 cm), with approximately 40 % of the total number of particles falls into the [2,3] μm range and a majority of 70 % falls into the [2–4] μm range. Additionally, due to the high evaporation rate of Acetone, the obtained particles for this solution are highly porous and geometrically inconsistent (see Supplementary Materials S3 for high-resolution SEM captures). Despite the identical spray duration and sampling area, the total number of particles collected decreases as interelectrode distance increases (Fig. 7(h)). The particles are more likely to be deflected by surrounding by ion wind flow at higher interelectrode distances, causing the particles to spiral out of the electric field, resulting in sparser particle depositions (Supplementary Materials Fig. S2).

With the PVDF 3 % in Acetone 1:1 DMF solution, SEM images for $r_E = 8$ cm and $r_E = 12$ cm (Figs. 7(d) and (e)) show that there is a layer of polymeric materials between the conductive tape surface and the deposited particles. Because of the low evaporation rate of DMF, the solvent cannot completely evaporate before arriving at the collector. Therefore, the residual solvent accumulates, and dissolves polymeric particles previously deposited on the collector. This behaviour is not observed for the 16 cm case where deposited particles are distinctly visible on the collector's surface. Moreover, the dissolution of deposited particles due to residual solvent might have underestimated the number of collected particles in case $r_E = 12$ cm, leading to a negligible difference between the particle counts of $r_E = 12$ cm and $r_E = 16$ cm as shown in Fig. 7(h).

Unlike particles in Acetone from the previous case, particles in the Acetone-DMF solvent are more intact with no porosity observed in SEM images. This is due to the presence of DMF which reduces the overall evaporation rate. In terms of size, the acquired particles in $r_E = 12$ cm and $r_E = 16$ cm are distributed among [1,2] μm, [2,3] μm and [3,4] μm ranges. For $r_E = 8$ cm, a large number of sub-micro (< 1 μm) particles was found, and majority of particles distributing over the [1,4] μm range. This behaviour can be explained by the lack of deflection due to ion wind flow in smaller distances, i.e. $r_E = 8$ cm .

In addition, no particle can be observed in the case of PVDF 3 % in DMF. At all three interelectrode distances, SEM images yield a layer of polymeric substance created by the collective deposition and dissolution of solvent-rich droplets, as shown in Fig. 7(g). Thus, no analysis on the particle morphology can be conducted in this case.

Fig. 7(h) summarises the averaged particle size of the PVDF 3 % in Acetone and in Acetone 1:1 DMF at different interelectrode distances. Based on this graph and previous results, the interelectrode distance does not have a clear influence on the particle size or size distribution. However, it has considerable impacts on the number of deposited particles and residual solvent on the collector. The averaged particle sizes of the PVDF 3 % in Acetone is considerably higher than that in the mixed Acetone-DMF solvent. This finding agrees with literature where decreased evaporation rate elongates the charged jet and reduces the jet diameter [25,27] considering that jet diameter is closely related with particles' size due to local charge-to-mass ratio [50]. This has significant contributions to pulmonary drug delivery application of electrospray where smaller particles can deliver drugs to deeper parts of the lung [11]. Specifically, in all cases the majority of particles is within 1–5 μm which is considered the optimal range to reach the lower respiratory tract and deposit in the alveoli [51]. However, 7 % to 11 % of the particles in the PVDF 3 % in Acetone falls into >5 μm range, whereas only 3 %–6 % of the particles in the PVDF 3 % in Acetone 1:1 DMF yields this measurement. This could mean that the use of mixed Acetone and DMF solvents can offer a relatively higher deposition efficiency as particles with size larger than 5 μm may be trapped primarily in the mouth, throat, and upper airways [52].

Figs. 8(a) and 8(b) show the size distribution for the electrosprayed particles at 35°C and 45°C, respectively, whilst Fig. 8(c) plots the averaged particle size at three investigated temperatures. The higher temperature cases registered more than 80 % of particle falling into the [1,4] μm range which is slightly different from the result of the 25°C sprays shown in Fig. 7(d). Furthermore, there is fewer sub-micro particles detected at 35°C and 45°C compared to the 25°C result. These characteristics along with the averaged particle size graph in Fig. 8(c) suggest that higher evaporation rates due to higher temperatures induce larger particles. However, the increase in particle size among these cases is also influenced by the mechanical and electrical properties of the liquid, such as electrical conductivity, surface tension, and density. These factors are known to affect the jet diameter and potentially the induced particles' size, following an established scaling law [53],

$$d_j = \left(\frac{\rho \varepsilon_0 Q^3}{\kappa_e \sigma}\right)^{\frac{1}{6}}, \tag{17}$$

where ρ is density, ε_0 is electric permittivity of air, Q is flow rate, κ_e is

Table 2
Quantitative comparisons of Taylor-cone's dimensions between simulation and experiment.

Acetone	Simulation	Experiment	Deviation (%)
Cone length l_c (mm)	0.1498	0.1812	17.33
Cone angle φ_c (°)	92	80	15
Ethanol	Simulation	Experiment	Deviation (%)
Cone length l_c (mm)	0.1609	0.2193	26.63
Cone angle φ_c (°)	88	71	23.94
DMF	Simulation	Experiment	Deviation (%)
Cone length l_c (mm)	0.1681	0.18	6.61
Cone angle φ_c (°)	85	81	4.94

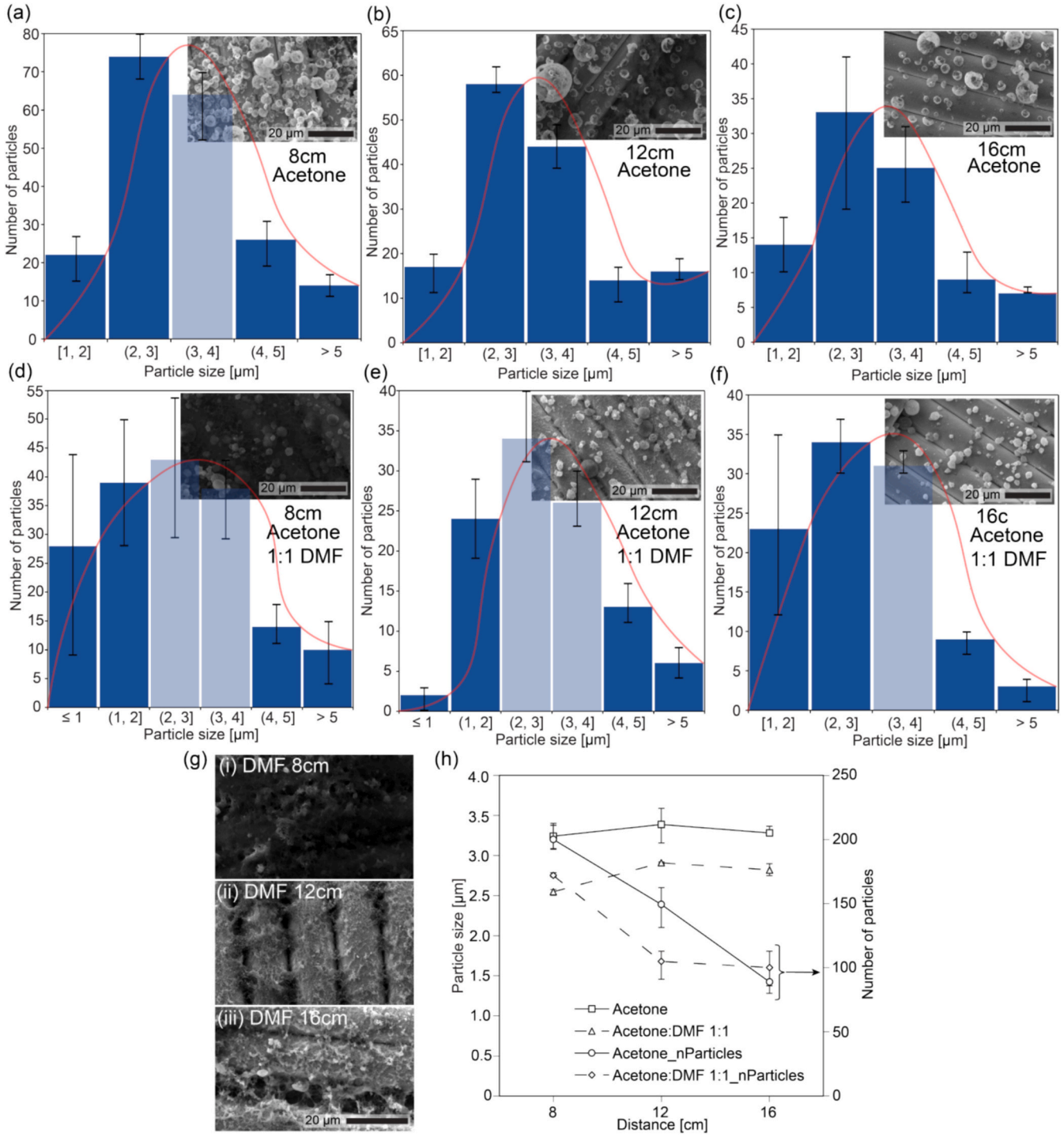

Fig. 7. Particle size distribution of electrospray of different polymeric solutions and interelectrode distance at room temperature (25 °C) with SEM images as insets; (a) PVDF 3 % in Acetone with 8 cm distance; (b) PVDF 3 % in Acetone with 12 cm distance; (c) PVDF 3 % in Acetone with 16 cm distance; (d) PVDF 3 % in Acetone 1:1 DMF with 8 cm distance; (e) PVDF 3 % in Acetone 1:1 DMF with 12 cm distance; (f) PVDF 3 % in Acetone 1:1 DMF with 16 cm distance; (g) SEM images of the particles electrosprayed with PVDF 3 % in DMF solution; and (h) averaged particle size dependence on polymeric liquids and interelectrode distance. Error bars indicate range of measured values for each data point.

electric conductivity and σ is surface tension. This law suggests that jet diameter is exponentially proportional to density and inversely proportional to conductivity and surface tension. The change of density with temperature for liquids is trivial and can be neglected, meanwhile conductivity of dielectric liquids is reported to increase with temperature, i.e. approximately 3 % to 8 % for $\mathring{1}$C temperature increase ($\kappa_e \propto T$) [54,55]. Surface tension is inversely proportional to temperature, with a decrease of roughly 0.2 % to 0.4 % for $\mathring{1}$C increase in temperature ($\sigma \propto \frac{1}{T}$) [56]. The change in these properties would collectively reduce the jet diameter as temperature rises. However, considering the exponent in Eq. 17 ($n=\frac{1}{6}$), the jet reduction effect might be insufficient and easily overwhelmed by the effect of increasing evaporation rate, thus resulting in the observed rise in particle size as shown in Fig. 8(c). Similar observations were reported by De Vrieze et al. where electrospun poly

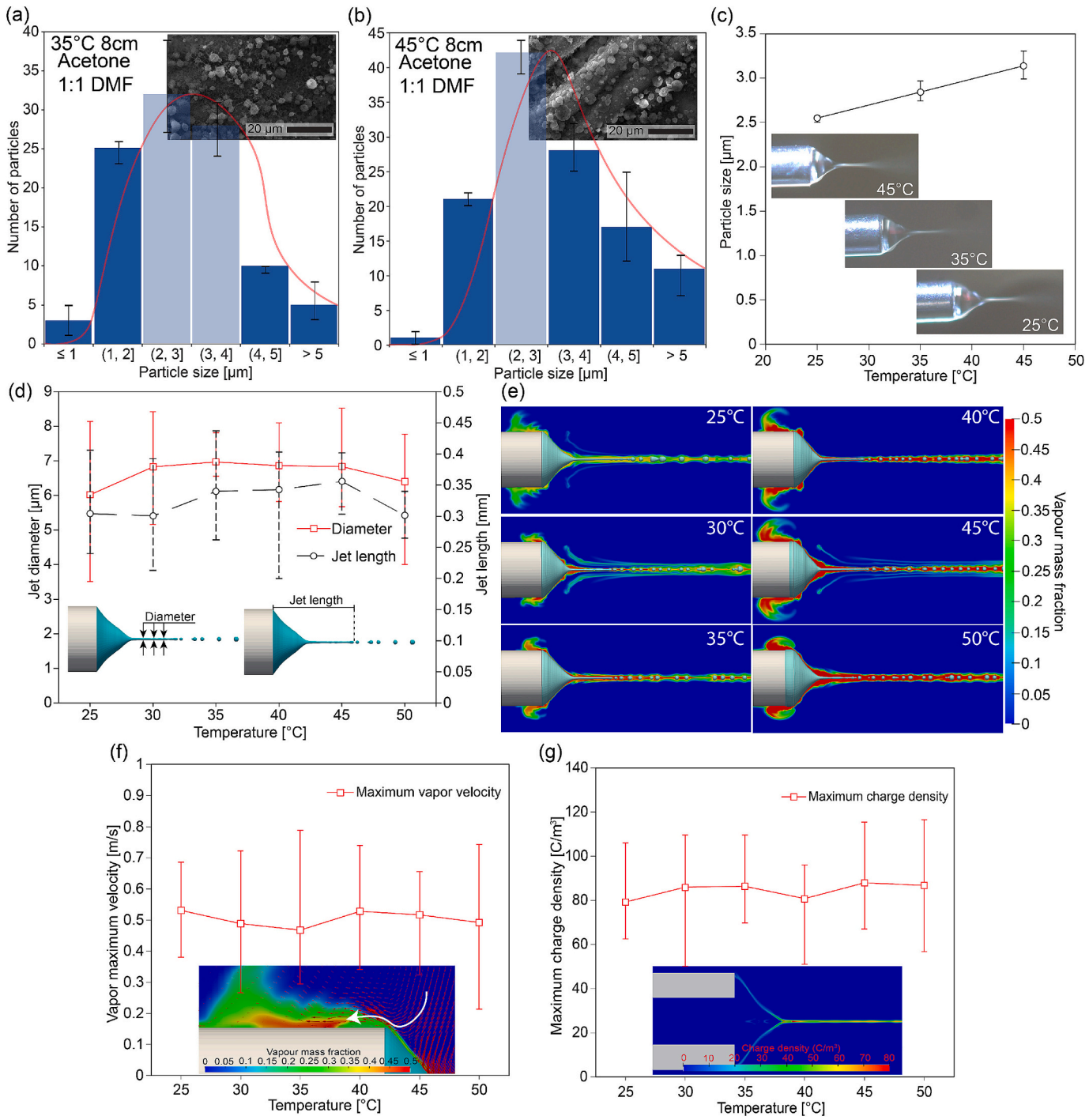

Fig. 8. Particle size distribution of electrospray of PVDF 3 % in Acetone 1:1 DMF solution with 8 cm distance at different liquid temperatures with SEM images as insets (a) PVDF 3 % in Acetone 1:1 DMF at 35 °C; (b) PVDF 3 % in Acetone 1:1 DMF at 45 °C; (c) Averaged particle size dependence liquid temperature; (d) Simulation results of jet's diameter and length; (e) Simulation results of Taylor-cone and jet with vapour field contour at different temperatures; Simulation results of (f) maximum velocity of vapour diffused from the electrospray liquid and (g) maximum charge density on the liquid-air interface. Error bars indicate range of measured values for each data point.

(vinylpyrrolidone) nanofibers increased in diameter as temperature rised [57], in which the authors briefly cited the dominant effect of evaporation over the variation in the rigidity of the polymer chains as the explanation for this finding.

From the insets of Fig. 8(c), the experimental captures of Taylor-cone and jet at the investigated temperatures show insignificant differences in the cone shape and jet length, which indicate the impact of evaporation rate on the particles is more prominent in the subsequent Coulomb fission process. This behaviour is supported by the simulated results in Fig. 8(d) (see Supplementary Materials S2 for more information on the measuring method of jet diameter and length). Similarly, simulations yield negligible impact of temperature on the diameter and length of the jet. Fig. 8(e) shows that there is no significant impact of temperatures on the shape of the Taylor-cone despite considerable differences in vapour field contour. The vapour field tends to concentrate in the vicinity of the liquid-air interface and cannot be dispersed due to the relatively steady

motion of the Taylor-cone and jet, decreasing the evaporation rate. In the subsequent Coulomb fission region, vapour field is dispersed due to the chaotic movement of particles and the ionic wind promoted by corona discharge [58], enhancing the evaporation rate. Simulations also yield negligible impact of temperatures on the maximum vapour diffusion velocity in the vicinity of the Taylor-cone (Fig. 8(f)) and maximum charge density on the Taylor-cone's liquid-air interface (Fig. 8(g)). The maximum vapour velocity correlation may imply that the evaporation rates among different temperatures are equalized by the localized vapour concentration, thus yielding similar values. The maximum charge density, which occurs at the throat of the Taylor-cone, potentially presents insignificant differences in charge behaviour within the Taylor-cone across these cases.

5. Conclusion

In conclusion, this study presents a comprehensive analysis of evaporation in electrohydrodynamic atomization, combining both numerical modelling and experimental validation. The proposed numerical model, based on the Taylor-Melcher leaky-dielectric model and the d^2 Law, successfully captured the geometric characteristics of the Taylor-cone and vapour field distribution. The findings highlight several important aspects: (i) the interelectrode distance has a negligible effect on particle size and morphology but it influences the solvent residue in deposited particles when solvents with medium to low volatility are used; (ii) higher evaporation rate reduces particle size; and (iii) while particle size is influenced by temperature, the evaporation process has minimal impact on the overall geometry of the Taylor-cone and jet due to the concentrated vapour field. Results also suggest that evaporation plays a more significant role in the Coulomb fission region, where vapour field disperses vigorously due to chaotic movement of particles and ion-wind generated by corona discharge, thus promoting solvent evaporation. These insights enhance the understanding of evaporation dynamics in electrohydrodynamic atomization and provide valuable guidelines for optimizing the process, especially in applications where controlling particle morphology and harmful solvent residue is necessary [10,11,59].

Supplementary data to this article can be found online at https://doi.org/10.1016/j.icheatmasstransfer.2025.109079.

CRediT authorship contribution statement

Ngoc Luan Mai: Writing – review & editing, Writing – original draft, Visualization, Validation, Software, Resources, Methodology, Investigation, Formal analysis, Data curation, Conceptualization. **Trung Hieu Vu:** Writing – review & editing, Writing – original draft, Methodology, Investigation. **Hoai-Duc Vu:** Writing – review & editing, Writing – original draft, Methodology, Investigation. **Canh Doan:** Writing – review & editing, Writing – original draft, Methodology, Investigation. **Yuen Yong:** Writing – review & editing, Writing – original draft, Supervision, Resources, Project administration, Funding acquisition, Formal analysis, Data curation. **Thien Xuan Dinh:** Writing – review & editing, Writing – original draft, Supervision, Software, Methodology. **Dzung Viet Dao:** Writing – review & editing, Writing – original draft, Validation, Project administration, Funding acquisition, Data curation, Conceptualization. **Van Thanh Dau:** Writing – review & editing, Writing – original draft, Supervision, Resources, Project administration, Methodology, Funding acquisition, Formal analysis, Data curation, Conceptualization.

Declaration of competing interest

The authors declare the following financial interests/personal relationships which may be considered as potential competing interests:

Van Thanh Dau reports financial support was provided by Australian Research Council. If there are other authors, they declare that they have no known competing financial interests or personal relationships that could have appeared to influence the work reported in this paper.

Acknowledgement

This work was supported by the Australian Research Council under grants DP230100637 and DP240101559, by the Griffith University Gowonda HPC Cluster and with the assistance of resources from the National Computational Infrastructure (NCI Australia), an NCRIS enabled capability supported by the Australian Government. N.L.M would like to thank Prof. Peter Woodfield for assisting with the revision.

Data availability

The data that support the findings of this study are available from the corresponding author upon reasonable request.

References

[1] Y. Man, C. Zhou, B. Adhikari, Y. Wang, T. Xu, B. Wang, High voltage electrohydrodynamic atomization of bovine lactoferrin and its encapsulation behaviors in sodium alginate, J. Food Eng. 317 (2022) 110842, https://doi.org/10.1016/j.jfoodeng.2021.110842.

[2] E.D. Khosroshahi, S.H. Razavi, H. Kiani, A. Aghakhani, Mixed fermentation and electrospray drying for the development of a novel stabilized wheat germ powder containing highly viable probiotic cultures, Food Sci. Nutr. 11 (5) (2023) 2176–2185, https://doi.org/10.1002/fsn3.3092.

[3] D. Fredrich, E. Weiand, A. Giusti, Electrostatic fields for the control of evaporating charged fuel sprays, Int. J. Multiphase Flow 160 (2023) 104312, https://doi.org/10.1016/j.ijmultiphaseflow.2022.104312.

[4] N. Chen, Y. Gan, Y. Luo, Z. Jiang, A review on the technology development and fundamental research of electrospray combustion of liquid fuel at small-scale, Fuel Process. Technol. 234 (2022) 107342, https://doi.org/10.1016/j.fuproc.2022.107342.

[5] S. Maharaj, M. Yunus Malik, O. Allegre, K. Lucy Smith, Computationally examining the effect of plate thickness on hole-emitter-type electrospray thrusters, J. Propuls. Power (2022) 1–9, https://doi.org/10.2514/1.B38767.

[6] P. Mallalieu, M. Jugroot, Multimodal electrospray thruster for small spacecraft: design and experimental characterization, J. Electr. Propuls. 3 (1) (2024) 12, https://doi.org/10.1007/s44205-024-00075-0.

[7] R. Yakut, K. Yakut, E. Sabolsky, J. Kuhlman, Experimental determination of cooling and spray characteristics of the water electrospray, Int. Commun. Heat Mass Transfer 120 (2021) 105046, https://doi.org/10.1016/j.icheatmasstransfer.2020.105046.

[8] Y. Kim, S. Jung, S. Kim, S.T. Choi, M. Kim, H. Lee, Heat transfer performance of water-based electrospray cooling, Int. Commun. Heat Mass Transfer 118 (2020) 104861, https://doi.org/10.1016/j.icheatmasstransfer.2020.104861.

[9] P.R. Patel, D. Haemmerich, Review on electrospray nanoparticles for drug delivery: exploring applications, Polym. Adv. Technol. 35 (7) (2024) e6507, https://doi.org/10.1002/pat.6507.

[10] T.-H. Vu, et al., Charge-reduced particles via self-propelled Electrohydrodynamic atomization for drug delivery applications, ACS Appl. Mater. Interfaces 15 (25) (2023) 29777–29788, https://doi.org/10.1021/acsami.3c02000.

[11] H.-D. Vu, et al., In-flight electro-neutralisation electrospray for pulmonary drug delivery, Nano Today 55 (2024) 102217, https://doi.org/10.1016/j.nantod.2024.102217.

[12] J. Xue, T. Wu, Y. Dai, Y. Xia, Electrospinning and Electrospun Nanofibers: methods, materials, and applications, Chem. Rev. 119 (8) (2019) 5298–5415, https://doi.org/10.1021/acs.chemrev.8b00593.

[13] C. Voniatis, et al., Co-electrospun polysuccinimide/poly(vinyl alcohol) composite meshes for tissue engineering, J. Mol. Liq. 306 (2020) 112895, https://doi.org/10.1016/j.molliq.2020.112895.

[14] X. Qin, S. Subianto, 17 - Electrospun nanofibers for filtration applications, in: M. Afshari (Ed.), Electrospun Nanofibers, Woodhead Publishing, 2017, pp. 449–466.

[15] T. Dinh, et al., Advances in rational design and materials of high-performance stretchable electromechanical sensors, Small 16 (14) (2020) 1905707, https://doi.org/10.1002/smll.201905707.

[16] M. Gorji, R. Bagherzadeh, H. Fashandi, 21 - Electrospun nanofibers in protective clothing, in: M. Afshari (Ed.), Electrospun Nanofibers, Woodhead Publishing, 2017, pp. 571–598.

[17] J. W. Fastier-Wooller *et al.*, "Flexible Iron-on sensor embedded in smart sock for gait event detection," ACS Appl. Mater. Interfaces, vol. 16, no. 1, pp. 1638–1649, 2024/01/10 2024, doi: https://doi.org/10.1021/acsami.3c11805.

[18] J.W. Fastier-Wooller, et al., Multimodal fibrous static and dynamic tactile sensor, ACS Appl. Mater. Interfaces 14 (23) (2022) 27317–27327, https://doi.org/10.1021/acsami.2c08195.

[19] J. Zhu, et al., Recent developments of electrospun nanofibers for electrochemical energy storage and conversion, Energy Storage Mater. 65 (2024) 103111, https://doi.org/10.1016/j.ensm.2023.103111.

[20] K.R.S. Dinuwan Gunawardhana, et al., The potential of Electrospinning to enable the realization of energy-autonomous wearable sensing systems, ACS Nano 18 (4) (2024) 2649–2684, https://doi.org/10.1021/acsnano.3c09077.
[21] N. Farjam, I.A. Spiegel, K. Barton, High-fidelity modeling and validation of Electrohydrodynamic jet printing, Materialia 26 (2022) 101578, https://doi.org/10.1016/j.mtla.2022.101578.
[22] K. Tang, R.D. Smith, Theoretical prediction of charged droplet evaporation and fission in electrospray ionization22Dedicated to professor Michael T. Bowers on the occasion of his 60th birthday, Int. J. Mass Spectrom. 185-187 (1999) 97–105, https://doi.org/10.1016/S1387-3806(98)14107-6.
[23] J.N. Smith, R.C. Flagan, J.L. Beauchamp, Droplet evaporation and discharge dynamics in electrospray ionization, Chem. Eur. J. 106 (42) (2002) 9957–9967, https://doi.org/10.1021/jp025723e.
[24] O. Wilhelm, L. Mädler, S.E. Pratsinis, Electrospray evaporation and deposition, J. Aerosol Sci. 34 (7) (2003) 815–836, https://doi.org/10.1016/S0021-8502(03)00034-X.
[25] S. Tripatanasuwan, Z. Zhong, D.H. Reneker, Effect of evaporation and solidification of the charged jet in electrospinning of poly(ethylene oxide) aqueous solution, Polymer 48 (19) (2007) 5742–5746, https://doi.org/10.1016/j.polymer.2007.07.045.
[26] Y. Cai, M. Gevelber, The effect of relative humidity and evaporation rate on electrospinning: fiber diameter and measurement for control implications, J. Mater. Sci. 48 (22) (2013) 7812–7826, https://doi.org/10.1007/s10853-013-7544-x.
[27] H.M. Golecki, et al., Effect of solvent evaporation on Fiber morphology in rotary jet spinning, Langmuir 30 (44) (2014) 13369–13374, https://doi.org/10.1021/la5023104.
[28] F. Meng, Y. Jiang, Z. Sun, Y. Yin, Y. Li, Electrohydrodynamic liquid atomization of biodegradable polymer microparticles: effect of electrohydrodynamic liquid atomization variables on microparticles, J. Appl. Polym. Sci. 113 (1) (2009) 526–534, https://doi.org/10.1002/app.30107.
[29] M. Jafari-Nodoushan, J. Barzin, H. Mobedi, Size and morphology controlling of PLGA microparticles produced by electro hydrodynamic atomization, Polym. Adv. Technol. 26 (5) (2015) 502–513, https://doi.org/10.1002/pat.3480.
[30] T.-H. Vu, et al., Enhanced Electrohydrodynamics for Electrospinning a highly sensitive flexible Fiber-based piezoelectric sensor, ACS Appl. Electron. Mater. 4 (3) (2022) 1301–1310, https://doi.org/10.1021/acsaelm.2c00030.
[31] Y. Li, et al., Molecular dynamics simulation of evaporation of electrified liquid in electrospray, Int. Commun. Heat Mass Transfer 155 (2024) 107502, https://doi.org/10.1016/j.icheatmasstransfer.2024.107502.
[32] K. Yamamoto, 10 - Optical visualization of acoustic fields: the schlieren technique, the Fresnel method and the photoelastic method applied to ultrasonic transducers, in: K. Nakamura (Ed.), Ultrasonic Transducers, Woodhead Publishing, 2012, pp. 314–328.
[33] J.L. Chaloupka, M. Woods, J. Aas, J. Hutchins, J.D. Thistle, Color Schlieren imaging with a two-path, double knife edge system, Opt. Express 22 (7) (2014) 8041–8046, https://doi.org/10.1364/OE.22.008041.
[34] J.D. Chapman, P.A. Kottke, A.G. Fedorov, Droplet-gas interactions in nanoelectrospray multiphase flow, Int. J. Multiphase Flow 172 (2024) 104701, https://doi.org/10.1016/j.ijmultiphaseflow.2023.104701.
[35] H.-I. Li, G.R.D. Prabhu, K. Buchowiecki, P.L. Urban, High-speed Schlieren imaging of vapor formation in electrospray plume, J. Am. Soc. Mass Spectrom. 35 (2) (2024) 244–254, https://doi.org/10.1021/jasms.3c00345.
[36] J.R. Melcher, G.I. Taylor, Electrohydrodynamics: a review of the role of interfacial shear stresses, Annu. Rev. Fluid Mech. 1 (1969) 35.
[37] L.N. Mai, et al., Numerical study of electrohydrodynamic atomization considering liquid wetting and corona discharge effects, Phys. Fluids 35 (6) (2023) 062014, https://doi.org/10.1063/5.0151085.
[38] D. Téré, et al., Evaporation and combustion of a drop of liquid fuel—a review, Smart Grid Renew. Energy 13 (2) (2022) 26, https://doi.org/10.4236/sgre.2022.132003.
[39] J.U. Brackbill, D.B. Kothe, C. Zemach, A continuum method for modeling surface tension, J. Comput. Phys. 100 (2) (1992) 335–354, https://doi.org/10.1016/0021-9991(92)90240-Y.
[40] C.W. Hirt, B.D. Nichols, Volume of fluid (VOF) method for the dynamics of free boundaries, J. Comput. Phys. 39 (1) (1981) 201–225, https://doi.org/10.1016/0021-9991(81)90145-5.
[41] H. Huh, R.E. Wirz, Simulation of electrospray emission processes for low to moderate conductivity liquids, Phys. Fluids 34 (11) (2022) 112017, https://doi.org/10.1063/5.0120737.
[42] G. Tomar, et al., Two-phase electrohydrodynamic simulations using a volume-of-fluid approach, J. Comput. Phys. 227 (2) (2007) 1267–1285, https://doi.org/10.1016/j.jcp.2007.09.003.
[43] J.R. Melcher, Continuum Electromechanics, no. Accessed from, https://nla.gov.au/nla.cat-vn1542161.
[44] J.C. Bénet, S. Ouoba, F. Ouedraogo, F. Cherblanc, Experimental study of water evaporation rate, at the surface of aqueous solution, under the effect of a discontinuity of chemical potential – effect of water activity and air pressure, Exp. Thermal Fluid Sci. 121 (2021) 110233, https://doi.org/10.1016/j.expthermflusci.2020.110233.
[45] O. Laguerre, L. Lecoq, F. Zoz, S. Guyot, L. Beney, D. Flick, Influence of the air humidity on the drying of a liquid droplet on a solid plate and on bacterial destruction, J. Food Eng. 212 (2017) 76–86, https://doi.org/10.1016/j.jfoodeng.2017.05.014.
[46] B. Stiehl, et al., The effect of relative air humidity on the evaporation timescales of a human sneeze, AIP Adv. 12 (7) (2022) 075210, https://doi.org/10.1063/5.0102078.
[47] G.I. Taylor, Disintegration of water drops in an electric field, Proc. R. Soc. Lond. 280 (1382) (1997) 383–397, https://doi.org/10.1098/rspa.1964.0151.
[48] M.J. Hargather, G.S. Settles, A comparison of three quantitative Schlieren techniques, Opt. Lasers Eng. 50 (1) (2012) 8–17, https://doi.org/10.1016/j.optlaseng.2011.05.012.
[49] F. Dalla Barba, J. Wang, F. Picano, Revisiting D2-law for the evaporation of dilute droplets, Phys. Fluids 33 (5) (2021) 051701, https://doi.org/10.1063/5.0051078.
[50] H. Wan, P.J. Liu, F. Qin, X.G. Wei, G.Q. He, W.Q. Li, Mechanisms of electrospray jet formation and atomized droplet motion in pulsed-jet mode, Phys. Fluids 36 (8) (2024) 087107, https://doi.org/10.1063/5.0214534.
[51] M.L. Jagrosse, D.A. Dean, A. Rahman, B.L. Nilsson, RNAi therapeutic strategies for acute respiratory distress syndrome, Transl. Res. 214 (2019) 30–49, https://doi.org/10.1016/j.trsl.2019.07.011.
[52] S.E. Maloney Norcross, L.P.K. Levin, A.J. Hickey, D.B. Hill, Biopolymeric inhalable dry powders for pulmonary drug delivery, Pharmaceuticals 17 (12) (2024), https://doi.org/10.3390/ph17121628.
[53] A.M. GaÑÁN-Calvo, On the general scaling theory for electrospraying, J. Fluid Mech. 507 (2004) 203–212a, https://doi.org/10.1017/S0022112004008870.
[54] B. Abedian, K.N. Baker, Temperature effects on the electrical conductivity of dielectric liquids, IEEE Trans. Dielectr. Electr. Insul. 15 (3) (2008) 888–892, https://doi.org/10.1109/TDEI.2008.4543127.
[55] J. Vila, et al., Temperature dependence of the electrical conductivity in EMIM-based ionic liquids: evidence of Vogel–Tamman–Fulcher behavior, Fluid Phase Equilib. 242 (2) (2006) 141–146, https://doi.org/10.1016/j.fluid.2006.01.022.
[56] N. Shardt, Y. Wang, Z. Jin, J.A.W. Elliott, Surface tension as a function of temperature and composition for a broad range of mixtures, Chem. Eng. Sci. 230 (2021) 116095, https://doi.org/10.1016/j.ces.2020.116095.
[57] S. De Vrieze, T. Van Camp, A. Nelvig, B. Hagström, P. Westbroek, K. De Clerck, The effect of temperature and humidity on electrospinning, J. Mater. Sci. 44 (5) (2009) 1357–1362, https://doi.org/10.1007/s10853-008-3010-6.
[58] N. Zehtabiyan-Rezaie, M. Saffar-Avval, K. Adamiak, On the evaporation enhancement from saline water due to corona discharge generated EHD flow: a numerical and experimental study, Int. Commun. Heat Mass Transfer 119 (2020) 104988, https://doi.org/10.1016/j.icheatmasstransfer.2020.104988.
[59] Y. Liu, K. Li, M.M. Mohideen, S. Ramakrishna, Chapter 1- development of melt electrospinning: the past, present, and future, in: Y. Liu, K. Li, M.M. Mohideen, S. Ramakrishna (Eds.), Melt Electrospinning, Academic Press, 2019, pp. 1–5.